FUGIN hot core survey. I. Survey method and initial results for $l = 10°–20°$

Kazuki Sato,[1,2,*,†] Tetsuo Hasegawa,[2] Tomofumi Umemoto,[3] Hiro Saito,[4] Nario Kuno,[4,5] Masumichi Seta,[6] and Seiichi Sakamoto[1,7]

[1]Department of Astronomy, Graduate School of Science, The University of Tokyo, 7-3-1 Hongo, Bunkyo-ku, Tokyo 133-0033, Japan

[2]National Astronomical Observatory of Japan, National Institutes of Natural Sciences, 2-21-1 Osawa, Mitaka, Tokyo 181-8588, Japan

[3]Nobeyama Radio Observatory, National Astronomical Observatory of Japan, National Institutes of Natural Sciences, Minamimaki, Minamisaku, Nagano 384-1305, Japan

[4]Department of Physics, Graduate School of Pure and Applied Sciences, University of Tsukuba, 1-1-1 Tennodai, Tsukuba, Ibaraki 305-8577, Japan

[5]Tomonaga Center for the History of the Universe, University of Tsukuba, 1-1-1 Tennodai, Tsukuba, Ibaraki 305-8571, Japan

[6]Department of Physics, School of Science and Technology, Kwansei Gakuin University, 2-1 Gakuen, Sanda, Hyogo 669-1337, Japan

[7]National Astronomical Observatory of Japan, National Institutes of Natural Sciences, Alonso de Córdova 3788, Office 61B, Vitacura, Santiago, Chile

*E-mail: kazuki.sato.ap@gmail.com

†Present address: Komatsu Ltd.

Abstract

We have developed a method to make a spectral-line-based survey of hot cores, which represent an important stage of high-mass star formation, and applied the method to the data of the FUGIN (FOREST Unbiased Galactic plane Imaging survey with the Nobeyama 45 m telescope) survey. First, we select hot core candidates by searching the FUGIN data for the weak hot core tracer lines (HNCO and CH_3CN) by stacking, and then we conduct follow-up pointed observations on these candidates in $C^{34}S$, SO, OCS, HC_3N, HNCO, CH_3CN, and CH_3OH $J = 2–1$ and $J = 8–7$ lines to confirm and characterize them. We applied this method to the $l = 10°–20°$ portion of the FUGIN data and identified 22 "HotCores" (compact sources with more than two significant detections of the hot core tracer lines, i.e., SO, OCS, HC_3N, HNCO, CH_3CN, or CH_3OH $J = 8–7$ lines) and 14 "DenseClumps" (sources with more than two significant detection of $C^{34}S$, CH_3OH $J = 2–1$, or the hot core tracer lines). The identified HotCores are found to be associated with signposts of high-mass star formation such as ATLASGAL clumps, WISE H II regions, and Class II methanol masers. Many of the FUGIN HotCores are identified with the Herschel Hi-GAL clumps with a median mass of $6.8 \times 10^2 \, M_\odot$ and a median bolometric luminosity of $7.4 \times 10^3 \, L_\odot$. Five of the seven HotCores with stronger CH_3CN lines exhibit elevated gas temperatures of 50–100 K. These observations suggest that FUGIN HotCores are closely related to the formation of stars with medium to high mass. For those associated with

ATLASGAL clumps, their bolometric luminosity to clump mass ratios are consistent with the star formation stages centered at the hot core phase. The catalog of FUGIN HotCores provides a useful starting point for further statistical studies and detailed observations of high-mass star forming regions.

Key words: ISM: clouds — ISM: molecules — radio lines: ISM — stars: formation — surveys

1 Introduction

High-mass stars play important roles in determining their environments on a galactic scale. They irradiate their surrounding gas and dust with strong UV light to heat and ionize them and drive stellar winds throughout their lifetime, and they finally explode as supernovae to have a significant impact even after the end of their lives. However, the process by which high-mass stars form is still under debate. It is important to study the early stages of their formation.

Often observed in high-mass star formation regions are "hot cores," which are hot (>100 K) and compact (<0.1 pc) cores of dense ($>10^7$ cm^{-3}) molecular gas with large bolometric luminosity ($L_{\rm bol} \sim 10^4$–$10^5 \, L_\odot$) and extinction ($A_v > 100$ mag) and characteristic chemistry (see, e.g., Hatchell et al. 2000; Nomura & Millar 2004; Wyrowski et al. 2006). In cool molecular clouds, gas-phase molecules are adsorbed on the surface of dust grains to form a mantle. Chemical reactions occur in both the mantles and the gas phase; molecules forming in ice mantles include complex organic molecules (e.g., Yamamoto 2017).

When high-mass stars are formed, surrounding dust grains are irradiated and become hot. Molecules in ice mantles evaporate to the gas phase. Hot cores are observed with the characteristic emission lines of molecules that evaporate from the grains.

One of the key questions in research into high-mass star formation is the conditions required to form high-mass stars. Statistical studies of high-mass star forming regions are essential to address this issue. Surveys of high-mass star formation regions are mainly conducted in dust continuum emission. For instance, toward the clumps identified by the APEX Telescope Large Area Survey of the Galaxy (ATLASGAL), which is an $870 \, \mu$m survey of the Galactic plane, spectral-line follow-ups have been made (Urquhart et al. 2018). Similarly, a search for dense gas in CS $J = 2$–1 emission was conducted toward IRAS point sources as an H II region survey (Bronfman et al. 1996). H II region catalogs of the Galactic plane were made using mid-infrared emission detected by the WISE satellite (Anderson et al. 2014) and by selecting compact sources in $70 \, \mu$m from the Hi-GAL (Herschel infrared Galactic Plane Survey) source catalog (Molinari et al. 2016).

These continuum-based surveys have, however, potential weak points. First, the millimeter/submillimeter dust continuum emission is roughly proportional to the product of dust column density and dust temperature. The continuum-based surveys thus naturally pick more massive cores relative to the less massive hot cores because of the larger range of dust column densities than dust temperatures. Secondly, source confusion can limit the separation of cores in crowded areas such as cluster-forming regions because continuum observations cannot separate sources by radial velocities.

To overcome the above weakness, it is important to conduct an unbiased survey in emission lines of hot core tracer molecules. Here we utilize the archived data of the FOREST Unbiased Galactic plane Imaging survey with the Nobeyama 45 m telescope (FUGIN), which is a survey of the Galactic plane in $l = 10°$–$50°$ and $198°$–$236°$, $b \leq \pm 1°$, using ^{12}CO, ^{13}CO, and C^{18}O $J = 1$–0 lines with additional lines in the frequency band. The velocity resolution of FUGIN is 1.3 km s^{-1}. The beam size is $14''$ and the angular resolution is $21''$ for ^{13}CO and C^{18}O (Umemoto et al. 2017). Since FUGIN is the Galactic plane CO survey made at the highest spatial resolution so far, it is most suited to finding compact sources such as hot cores. Although FUGIN was targeted on the CO $J = 1$–0 lines, the observed frequency band includes some other weaker molecular lines such as HNCO $J_{K_a, K_c} = 5_{0,5}$–$4_{0,4}$ (109.906 GHz) and CH$_3$CN $J_K = 6_K$–5_K ($K = 0, 1, 2, 3$; 110.364–110.384 GHz), which are known as good tracers of hot cores. We used these lines to survey hot cores without bias to the continuum emission. This research is the first to approach a hot core survey using hot core tracer lines. We can discuss statistical characteristics of hot cores without a bias to bright continuum emission.

In this paper, we establish a method to select candidate hot cores from the survey data, followed by confirmation observations (section 2), and introduce initial results for the $l = 10°$–$20°$ area (section 3). In section 4, we characterize the nature of the detected sources.

2 Method

Our hot core survey based on the FUGIN data is comprised of two major steps. First, we search for hot core
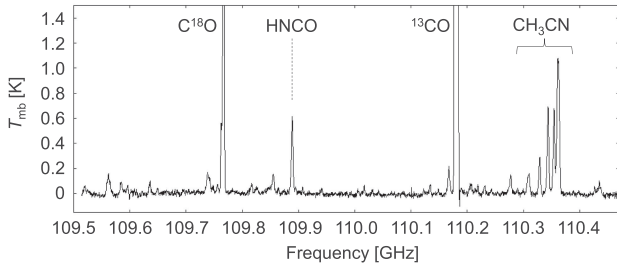
Fig. 1. Spectrum near the ^{13}CO and $C^{18}O$ $J = 1$–0 lines of W 51 e1/e8 taken during the FUGIN survey for calibration purposes.
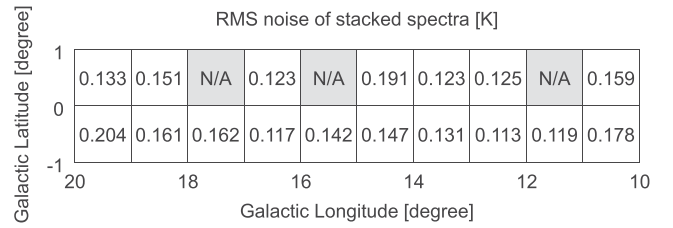

Fig. 2. The rms noise levels of the stacked specra at 110 GHz in each degree squared at 1.3 km s^{-1} velocity resolution. In the three regions $12° \leq l \leq 13°$, $0° \leq b \leq 1°$; $15° \leq l \leq 16°$, $0° \leq b \leq 1°$; and $17° \leq l \leq 18°$, $0° \leq b \leq 1°$ there are strong scanning effects and we did not extract hot core candidates from these regions.

candidates by looking at the $C^{18}O$, HNCO, and CH_3CN lines observed in the FUGIN survey. We then make pointed observations towards the candidate sources at higher sensitivity to confirm and characterize the sources. In the following, we describe these steps in detail.

2.1 Candidate selection

First, we analyze the FUGIN survey data (Umemoto et al. 2017) to search for hot core candidates. Figure 1 shows the spectrum of the hot core source W 51 e1/e8, which was observed repeatedly during the FUGIN survey for calibration purposes. In this high-sensitivity spectrum, we clearly see the emission lines of HNCO $J_{K_a,K_c} = 5_{0,5}$–$4_{0,4}$ and CH_3CN $J_K = 6_K$–5_K ($K = 0, 1, 2, 3, 4$) in addition to the ^{13}CO and $C^{18}O$ $J = 1$–0 lines. These HNCO and CH_3CN lines are known as tracers of hot cores (see, e.g., Bisschop et al. 2007).

The sensitivity of the actual FUGIN survey has been set for the ^{12}CO, ^{13}CO, and $C^{18}O$ lines, and the resultant rms noise is $dT_{mb} \approx 0.2$–0.4 K for the ^{13}CO and $C^{18}O$ lines. This makes it difficult to detect hot core tracer lines from the survey data if we depend on only one line of a hot core tracer molecule. To improve the signal-to-noise ratio, we stacked the HNCO $J_{K_a,K_c} = 5_{0,5}$–$4_{0,4}$ line and the four lines of CH_3CN $J_K = 6_K$–5_K ($K = 0, 1, 2, 3$). However, the stacked line is still not enough to exclude false detections from candidate sources for confirmation observations. Through our preliminary analysis of W 51 e1/e8, we found that real sources were always associated with relatively bright $C^{18}O$ emission [$T_{mb}(C^{18}O) \geq 1.5$ K], which indicates regions of high molecular gas column density. Since we can safely assume that hot cores exist in regions of high molecular column density, we require the hot core candidates to be associated with bright $C^{18}O$ emission. We thus selected our candidates in the following three steps:

1. In the $C^{18}O$ datacube, we identify positions with $T_{mb}(C^{18}O) \geq 1.5$ K and record the corresponding

peak velocities. By assuming the conditions typical for dense gas, this roughly corresponds to $N(H_2) \geq 8 \times 10^{23}$ cm^{-2}.

2. We calculate the integrated intensity of the stacked HNCO and CH_3CN lines over ± 5 km s^{-1} centered at the peak velocity of $C^{18}O$. If the integrated intensity exceeds 5σ, we regard it as a positive detection.

3. When we find more than two adjacent positive detections in the datacube, we regard them as a single source at the position where we get the strongest integrated intensity of the stacked lines.

We applied this method to the $10° \leq l \leq 20°$, $-1° \leq b \leq 1°$ part of the FUGIN data except for the regions $12° \leq l \leq 13°$, $0° \leq b \leq 1°$; $15° \leq l \leq 16°$, $0° \leq b \leq 1°$; and $17° \leq l \leq 18°$, $0° \leq b \leq 1°$, which have strong scanning noise and are not suitable for candidate selection. The rms level of each degree squared is 0.1–0.2 K in the T_{mb} scale, as shown in figure 2. We adopted this rms noise level to calculate the candidate selection threshold in each degree squared. Consequently, we analyzed the 17 degrees squared area of the FUGIN survey following the procedure described above and found 64 candidates for confirmation.

2.2 Confirmation observation

We focus on the characteristic chemical abundance of hot cores to identify the sources. In addition, we investigate the compactness of the molecular distribution to exclude shock-originated molecular lines.

We conducted observations towards the hot core candidates using the Nobeyama 45 m radio telescope in 2018 March and May. The four-beam receiver FOREST (Minamidani et al. 2016) and the autocorrelation spectrometer SAM45 (Kuno et al. 2011) were used. The RF frequency ranges were 94.8–96.8 GHz and 108.8–110.8 GHz in the lower and upper sidebands, respectively. The spectrometer was configured to cover 4 GHz in total at a

Table 1. List of important molecular lines included in the confirmation observation.
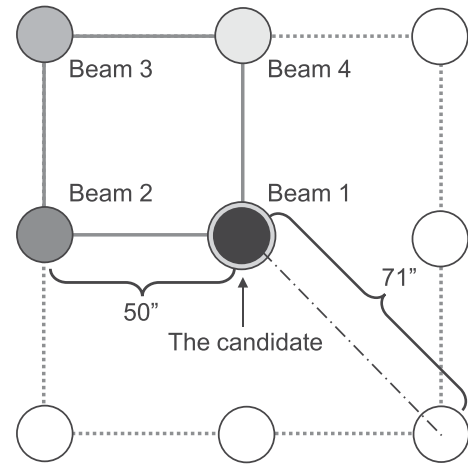
Molecule	Transition	Frequency [GHz]	E_u/k* [K]
$C^{18}O$	$J = 1–0$	109.782173	5.27
$C^{34}S$	$J = 2–1$	96.412950	6.94
SO	$J_K = 2_3–1_2$	109.252220	21.05
OCS	$J = 9–8$	109.463063	26.26
HC_3N	$J = 12–11$	109.173634	34.06
HNCO	$J_{K_a,K_c} = 5_{0,5}–4_{0,4}$	109.905749	15.82
CH_3CN	$J_K = 6_0–5_0$	110.383500	18.54
CH_3CN	$J_K = 6_1–5_1$	110.381372	25.68
CH_3CN	$J_K = 6_2–5_2$	110.374989	47.13
CH_3CN	$J_K = 6_3–5_3$	110.364354	82.85
CH_3CN	$J_K = 6_4–5_4$	110.349470	132.84
CH_3OH	$J_K = 2_0–1_0$ A^+	96.741371	6.96
CH_3OH	$J_K = 2_{-1}–1_{-1}$ E	96.739358	12.54
CH_3OH	$J_K = 2_0–1_0$ E	96.744545	20.09
CH_3OH	$J_K = 8_0–7_1$ A^+	95.169391	83.54

*E_u is the upper state energy.

Fig. 3. Mapping pattern of the confirmation observation with the four FOREST beams. We observed the candidate at the center with Beam 1, 2, 3, and 4 in turn to get spectra of the positions 50″ and 71″ away from the center.

3 Results

3.1 Identification of HotCores and DenseClumps

Figure 4 shows an example of the results of our follow-up observations. It shows the line profiles (upper panels) and integrated intensity distributions (lower panels) of the nine important molecular lines observed from one of the identified hot core sources, G10.300−0.144. For each molecular line, we see its line profile and its spatial extent in a bar graph showing the integrated intensities at the center and the positions 50″ and 71″ away from the center. The intensities at 50″ and 71″ offsets are averages of the intensities at the four positions, i.e., north, south, east, and west in Galactic coordinates at 50″ offset, and northeast, northwest, southeast, and southwest at 71″ offset (figure 3). The 1σ errors are shown by the solid lines at the top of the bars. The errors shown for the offset positions represent only the statistical errors and do not include the intrinsic intensity variation among the four positions in the average. With the exceptions of $C^{18}O$ $J = 1–0$ and CH_3CN lines, the line intensities are integrated over seven velocity channels ($V_{peak} − 4.9$ km s$^{-1} \leq V_{LSR} \leq V_{peak} + 4.9$ km s^{-1} at 96 GHz and $V_{peak} − 4.3$ km s$^{-1} \leq V_{LSR} \leq V_{peak} + 4.3$ km s^{-1} at 110 GHz) centered at the peak velocity of the $C^{18}O$ emission (V_{peak}). The $C^{18}O$ $J = 1–0$ line is integrated over 10 channels ($V_{peak} − 6.1$ km s$^{-1} \leq V_{LSR} \leq V_{peak} + 6.1$ km s^{-1}). In the case of CH_3CN, the strongest $J_K = 6_0–5_0$ line is blended with the neighboring $J_K = 6_1–5_1$ line, and a wider velocity range is used for integration ($V_{peak} − 3.7$ km s$^{-1} \leq V_{LSR} \leq V_{peak} + 8.5$ km s^{-1}) to include the $J_K = 6_1–5_1$ line.

We regard a line as detected if the integrated intensity exceeds 3σ and its profile has a reasonable shape centered

448.28 kHz channel separation. The corresponding velocity resolution varies from 1.52 km s^{-1} at 96 GHz to 1.33 km s^{-1} at 110 GHz. The beam size is 17″ at 96 GHz and 14″ at 110 GHz. The system noise temperatures were 150–350 K at 96 GHz and 200–400 K at 110 GHz during the observations. SiO masers were observed every 1 hr to calibrate the pointing offset of the telescope, and the pointing error was typically less than 3″.

The major spectral lines in the observed frequency ranges are listed in table 1. In addition to the $C^{18}O$ $J = 1–0$, HNCO $J_{K_a,K_c} = 5_{0,5}–4_{0,4}$, and CH_3CN $J = 6–5$ lines that we used to find the candidates, we observed $C^{34}S$ $J = 2–1$, SO $J_K = 2_3–1_2$, OCS $J = 9–8$, HC_3N $J = 12–11$, and CH_3OH lines, which are often quoted as tracers of hot cores. For CH_3OH, in addition to the $J_K = 2_0–1_0$ A^+, $J_K = 2_{-1}–1_{-1}$ E, and $J_K = 2_0–1_0$ E lines, we observed the $J_K = 8_0–7_1$ A^+ line, which is known to exhibit maser action in some high-mass star forming regions (see, e.g., Chen et al. 2011).

We observed the 64 candidates in position-switching mode using the FOREST four-beam receiver with the pattern shown in figure 3. The central position of a candidate was observed by the four beams in turn. As a result, we got a 3 × 3 map with a 50″ grid centered at each candidate. This allows us to judge whether or not the emission is spatially confined (≪100″ = 1.45 pc at 3 kpc), and to exclude extended objects not considered as hot cores from the hot core candidate list. The integration time was set to achieve a target sensitivity of $dT_{mb} \approx 0.03–0.05$ K, which was ∼10 times lower than that of the original FUGIN survey.
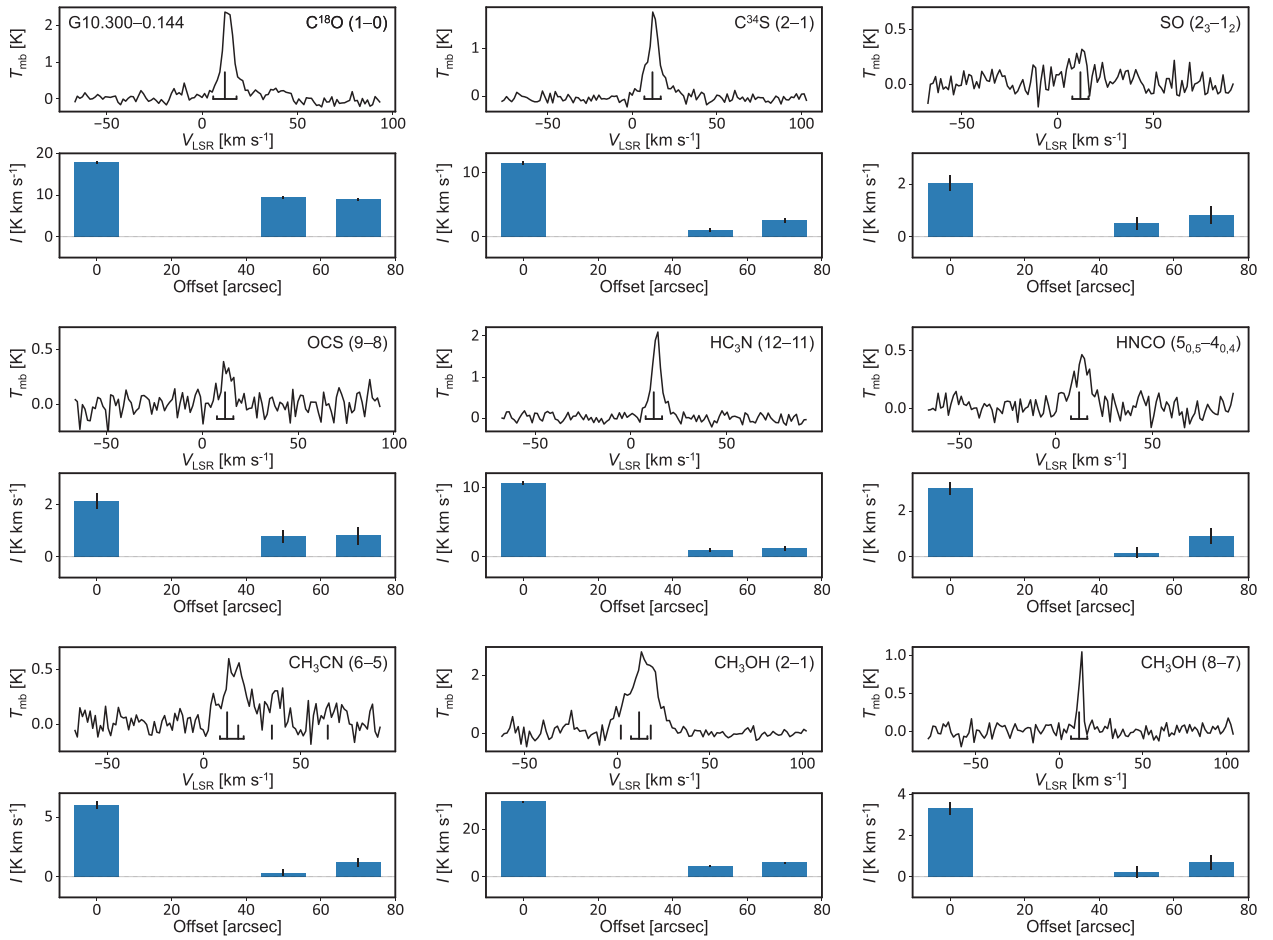
Fig. 4. Example of the results of the confirmation observations showing the profiles of nine molecular lines observed from G10.300−0.144. The upper part of each panel shows the line profile. The horizontal axis is the radial velocity, V_{LSR} (km s^{-1}), and the vertical axis is the main beam antenna temperature, T_{mb} (K). The long vertical lines indicate the peak velocity of the C^{18}O line, and the short vertical lines for the CH$_3$CN and CH$_3$OH lines correspond to the frequency of their weaker lines. The horizontal lines with ticks on both ends indicate the velocity range of integration. The lower side of each panel shows the integrated intensity of the line at the center, $I = \int T_{mb} \, dV$ (K km s^{-1}), and the average intensities at positions 50″ and 71″ away from the center. We can judge the compactness of the emission region by comparing these three intensities. (Color online)

at the source velocity defined by the C^{18}O line. The spatial compactness of the molecular emission is judged from a comparison of the integrated intensity at the center with those 50″ and 71″ away. At a distance of 3 kpc, 50″ corresponds to 0.73 pc, which is significantly larger than the typical size of a hot core, so detection of hot core tracer lines is expected only toward the center. In the example shown in figure 4, all of the nine molecular lines are detected, and their spatial distribution is compact except for C^{18}O.

The confirmation observation results of the 64 candidates show a range of significance for identification as a hot core. While we detect many of the spectral lines in table 1 from some candidates, other sources only show the C^{34}S and CH$_3$OH $J = 2$–1 lines besides C^{18}O. Based on the detected lines and their spatial distributions, we classify the candidates into three categories, "HotCores,"

"DenseClumps," and non-detections, with the following definitions.[1]

HotCores Sources with detection of at least two of the hot core lines (SO, OCS, HC$_3$N, HNCO, CH$_3$CN, CH$_3$OH $J = 8$–7) with clear spatial concentration at the center judged from a comparison of the line intensity at the center with those at positions 50″ and 71″ away from the center. G10.300−0.144 shown in figure 4 is a typical example of this category.

DenseClumps Sources that fail to meet the HotCore criteria, but with detection of at least two of C^{34}S, CH$_3$OH $J = 2$–1, or the hot core lines listed above.

---

[1] Since the definitions of the terms "HotCores" and "DenseClumps" used in this paper can be slightly different from the classical definitions, we write them in our definitions with capital letters.

Table 2. Identified HotCores and DenseClumps with integrated intensities.

Name	V_{LSR} [km s^{-1}]	Distance* [kpc]	C^{18}O 1–0	C^{34}S 2–1	SO 2_3–1_2	OCS 9 − 8	HC$_3$N 12 − 11	HNCO $5_{0,5}$–$4_{0,4}$	CH$_3$CN 6–5[†]	CH$_3$OH 2–1[‡]	CH$_3$OH 8–7[‡]
HotCores											
G10.145−0.339	10.6	3.12 ± 0.21	13.49	2.92	1.33	(−0.12)	(0.02)	1.11	(0.66)	4.88	(0.17)
G10.178−0.350	13.3	3.12 ± 0.21	23.29	6.49	(0.39)	(0.62)	3.93	1.92	(1.11)	7.14	(0.60)
G10.187−0.344	12.0	3.12 ± 0.21	22.65	2.09	(0.67)	1.31	1.85	2.91	(1.17)	11.22	(0.22)
G10.220−0.369	12.0	3.12 ± 0.21	26.02	1.89	(0.27)	(0.77)	1.43	2.43	(−0.11)	8.53	(0.09)
G10.300−0.144	12.0	3.13 ± 0.22	17.84	11.46	2.07	2.14	10.61	3.03	6.03	31.53	3.34
G10.465+0.034	72.0	$8.55^{+0.63}_{-0.55}$	11.21	2.27	0.84	(0.49)	1.83	2.99	0.87	12.40	(0.49)
G10.473+0.028	66.6	$8.55^{+0.63}_{-0.55}$	24.07	27.50	11.79	13.28	22.52	14.94	32.48	66.01	14.27
G10.481+0.036	66.6	$8.55^{+0.63}_{-0.55}$	10.92	2.96	1.33	1.51	3.96	6.79	2.92	29.96	2.41
G10.623−0.380	− 2.7	$4.95^{+0.51}_{-0.43}$	57.17	33.82	7.01	3.98	25.56	5.66	11.25	39.99	7.84
G11.920−0.616	36.0	$3.37^{+0.39}_{-0.32}$	12.80	4.55	1.24	2.41	8.63	6.12	6.30	39.33	8.76
G11.939−0.616	38.6	$3.37^{+0.39}_{-0.32}$	18.32	7.39	0.65	(0.74)	11.59	1.62	3.77	14.76	1.72
G12.416+0.510	18.6	1.83 ± 0.09	12.66	3.46	1.10	1.10	4.30	(0.69)	(0.66)	9.49	(0.70)
G12.680−0.176	56.0	$2.40^{+0.17}_{-0.15}$	26.91	2.32	(0.37)	(−0.04)	2.47	1.49	(0.43)	12.78	(0.45)
G12.810−0.204	34.6	$2.92^{+0.35}_{-0.28}$	48.73	27.96	3.95	2.27	20.78	3.42	5.70	28.83	2.88
G12.888+0.490	33.3	$2.50^{+0.28}_{-0.23}$	27.43	11.42	3.68	2.91	10.92	2.30	5.38	12.96	6.41
G13.185−0.109	53.3	4.60 ± 0.23	14.81	1.27	(0.26)	(−0.18)	2.41	1.64	1.54	11.19	(0.38)
G13.199−0.134	52.0	4.60 ± 0.23	16.17	1.02	(0.10)	(0.42)	0.81	1.55	(−0.37)	10.03	(−0.22)
G13.216+0.029	52.0	4.57 ± 0.22	14.66	1.00	(0.11)	0.80	1.29	1.82	0.93	13.71	0.95
G14.113−0.569	21.3	1.86 ± 0.10	15.24	2.13	1.60	(0.18)	1.33	(0.67)	1.56	5.02	(0.60)
G14.330−0.644	21.3	$1.12^{+0.14}_{-0.11}$	18.20	12.07	8.60	4.40	22.03	3.41	9.52	50.81	57.76
G14.636−0.569	18.6	$1.83^{+0.08}_{-0.07}$	9.64	2.65	0.48	(0.30)	2.77	0.91	0.91	15.57	1.43
G19.367−0.041	26.6	3.11 ± 0.26	14.47	2.62	0.48	1.00	0.56	(0.24)	(−0.13)	10.05	(0.57)
DenseClumps											
G10.131−0.408	10.6	3.12 ± 0.21	12.69	0.96	(0.00)	(−0.48)	(0.12)	(0.56)	(−0.28)	4.60	(−0.08)
G10.195−0.397	10.6	3.12 ± 0.21	20.23	1.74	(−0.23)	(−0.03)	1.12	(0.74)	(0.03)	5.83	(0.04)
G10.203−0.341	12.0	3.12 ± 0.21	24.38	1.79	(−0.06)	(0.90)	(1.07)	0.98	0.58	7.02	(0.43)
G10.203−0.308	10.6	3.12 ± 0.21	18.60	(0.93)	(0.26)	(0.18)	(0.43)	1.54	(1.10)	2.08	(0.54)
G10.209−0.336	12.0	3.12 ± 0.21	28.21	1.73	(0.33)	(0.23)	1.67	2.04	(0.32)	7.84	(0.61)
G10.631−0.372	− 1.4	$4.95^{+0.51}_{-0.43}$	17.46	3.25	(−0.21)	(0.43)	2.41	(0.79)	(0.15)	5.73	(0.75)
G11.059−0.372	− 1.4	4.91 ± 0.25	12.70	(0.32)	(0.26)	(0.37)	(−0.06)	0.83	(0.14)	2.07	(−0.25)
G11.109−0.388	0.0	4.91 ± 0.25	10.83	0.55	(−0.12)	(0.14)	(0.10)	(0.31)	(0.15)	2.82	(−0.02)
G12.685−0.171	54.6	$2.40^{+0.17}_{-0.15}$	18.89	1.19	(−0.09)	(0.00)	0.74	0.86	(0.01)	6.18	(0.22)
G12.816−0.185	34.6	$2.92^{+0.35}_{-0.28}$	19.23	5.33	(0.35)	0.72	4.52	2.37	2.31	24.47	1.09
G12.855−0.201	36.0	$2.92^{+0.35}_{-0.28}$	17.08	1.16	(−0.14)	(−0.21)	0.78	(0.41)	(0.70)	2.37	(−0.13)
G12.911+0.487	32.0	$2.50^{+0.28}_{-0.23}$	13.81	1.64	(−0.54)	(0.00)	(0.81)	(0.79)	(−1.07)	3.35	(0.64)
G13.202+0.057	52.0	4.57 ± 0.22	12.17	1.13	(0.16)	(−0.06)	0.88	(0.68)	(0.82)	2.35	(0.14)
G14.202−0.199	38.6	3.09 ± 0.39	13.02	1.55	(−0.10)	(0.04)	(0.14)	(0.34)	(0.93)	8.88	(0.11)

*See subsection 3.3 for the methods of distance determination.

[†]This column shows the integrated intensities of the blend of the CH$_3$CN $J_K = 6_0$–5_0 and $J_K = 6_1$–5_1 lines.

[‡]The column of CH$_3$OH $J = 2$–1 shows the integrated intensities of the blend of the $J_K = 2_0$–1_0 A$^+$ and $J_K = 2_{-1}$–1_{-1} E lines, and the column of CH$_3$OH $J = 8$–7 shows the integrated intensities of the $J_K = 8_0$–7_1 A$^+$ line.

[§]The intensities in parentheses are below the 3σ detection thresholds.

Non-detections Candidates that do not meet the criteria for the above two categories are not considered as positive detections. Most of them may represent the inevitable false positive detections in the candidate selection step.

We identified 22 HotCores and 14 DenseClumps, which represent 34% (HotCores) and 22% (DenseClumps) of the observed 64 candidates. Table 2 shows the identified Hot-Cores and DenseClumps according to the above criteria. The method for estimating the distance of each candidate is described in subsection 3.3. The intensities in parentheses in table 2 are those below the 3σ detection thresholds. Many of the DenseClumps are detected only in C^{34}S and CH$_3$OH $J = 2$–1. We classify G10.203−0.341, G10.209−0.336,
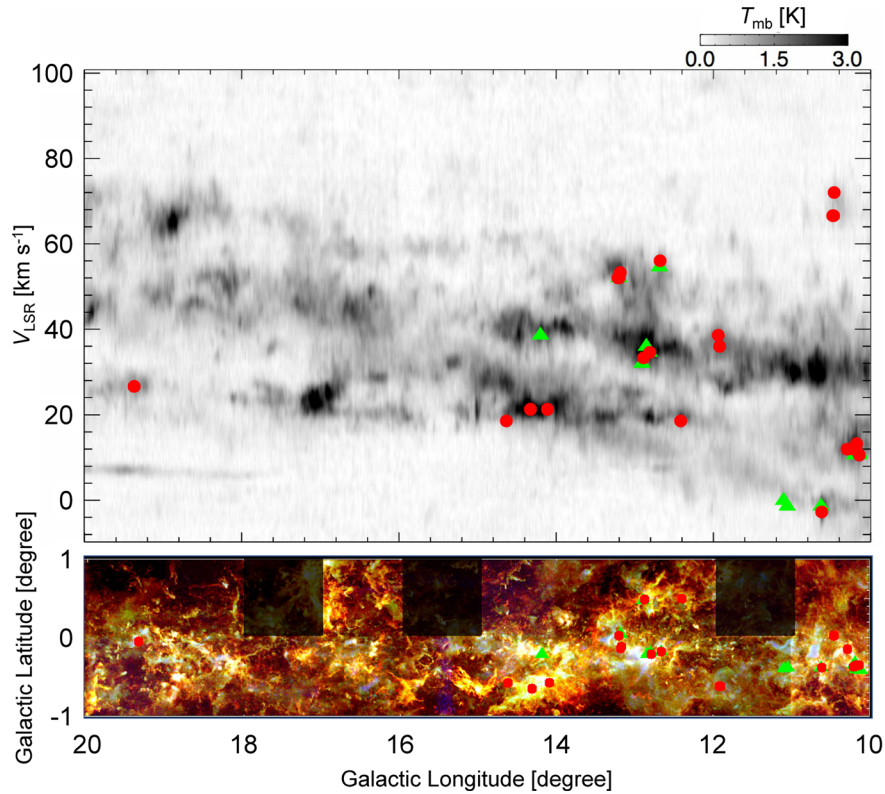
Fig. 5. HotCores and DenseClumps distribution on FUGIN ^{13}CO longitude–velocity diagram and CO image. Upper panel: HotCores (red circles) and DenseClumps (green triangles) distribution on ^{13}CO longitude–velocity diagram. Lower panel: HotCores and DenseClumps distribution on the FUGIN three-color image of CO peak intensities (red: ^{12}CO; green: ^{13}CO; blue: C^{18}O). The three shaded squares indicate the regions where we did not extract hot core candidates due to bad signal-to-noise ratio. The noise level is different in each square, as shown in figure 2. (Color online)

and G12.816−0.185 as DenseClumps despite the multiple detection of hot core lines, because their spatial distributions of the line intensities are not concentrated.

We note that the criteria employed in this work to identify HotCores do not explicitly include direct indices of high gas temperature (e.g., ~100 K or higher). In this respect, the definition of HotCores in this paper may be broader than the classical definition, and the HotCores identified here can also include the warm envelopes with similar chemical characteristics that surround forming high-mass stars. An analysis of the excitation temperatures of CH$_3$CN and CH$_3$OH is being planned to further explore this point, but it is outside the scope of the present paper.

extent. The groups have 2–9 members with spatial extents of ~1–10 pc and radial velocity extents of ~1–5 km s^{-1}. The spatial extent and velocity spreads are consistent with the size–linewidth relationship found in the interstellar medium (Larson 1981). This supports the idea that the members belongs to the same molecular cloud and are not artifacts due to line-of-site projection. The groups listed in table 3 include 29 (81%) out of the 36 sources including both HotCores and DenseClumps. If we count only those identified as HotCores, 16 (73%) out of 22 HotCores are in 6 groups. This indicates that the formation process of high-mass stars proceeds concurrently at multiple locations within this spatial scale of ~1–10 pc, i.e., within a molecular cloud.

3.2 Clustering of HotCores

Figure 5 shows the distribution of HotCores and DenseClumps overlaid on the FUGIN three-color image of the ^{12}CO/^{13}CO/C^{18}O peak intensities and the ^{13}CO l–V diagram. We immediately note that many of the identified HotCores and DenseClumps are clustered in space and velocity. Table 3 shows the 10 groups with more than two members, with their distances (see subsection 3.3) and spatial

3.3 Distance estimates

We estimate the distances in tables 2 and 3 in the following way. Eight of the HotCores are associated with maser sources with trigonometric parallax measurements: Sanna et al. (2014) for G10.473+0.028 and G10.623−0.380; Sato et al. (2014) for G11.920−0.616; Immer et al. (2013) for G12.680−0.176 and G12.810−0.204; Xu et al. (2011) for G12.888+0.490; Sato et al. (2010) for G14.330−0.644;

Table 3. Groups of the FUGIN HotCores and DenseClumps.[*]

Group name[†]	Member	V_{LSR} [km s^{-1}]	Category[‡]	Distance[§] [kpc]	Spatial extent l [pc] $\times$ b [pc]
G10.18−0.35	G10.131−0.408	10.6	DC	3.12 ±0.21	9.3 × 5.5
	G10.145−0.339	10.6	HC		
	G10.178−0.350	13.3	HC		
	G10.187−0.344	12.0	HC		
	G10.195−0.397	10.6	DC		
	G10.203−0.341	12.0	DC		
	G10.203−0.308	10.6	DC		
	G10.209−0.336	12.0	DC		
	G10.220−0.369	12.0	HC		
G10.47+0.03	G10.465+0.034	72.0	HC	$8.55^{+0.63}_{-0.55}$	2.4 × 2.4
	G10.473+0.028	66.6	HC		
	G10.481+0.036	66.6	HC		
G10.62−0.38	G10.623−0.380	−2.7	HC	$4.95^{+0.51}_{-0.43}$	0.7 × 1.7
	G10.631−0.372	−1.4	DC		
G11.11−0.39	G11.059−0.372	−1.4	DC	4.91 ±0.25	4.3 × 1.4
	G11.109−0.388	0.0	DC		
G11.92−0.62	G11.920−0.616	36.0	HC	$3.37^{+0.39}_{-0.32}$	1.1 × 0.0
	G11.939−0.616	38.6	HC		
G12.68−0.18	G12.680−0.176	56.0	HC	$2.40^{+0.17}_{-0.15}$	0.2 × 0.2
	G12.685−0.171	54.6	DC		
G12.81−0.20	G12.810−0.204	34.6	HC	$2.92^{+0.35}_{-0.28}$	2.3 × 1.0
	G12.816−0.185	34.6	DC		
	G12.855−0.201	36.0	DC		
G12.89+0.49	G12.888+0.490	33.3	HC	$2.50^{+0.28}_{-0.23}$	1.0 × 0.9
	G12.911+0.487	32.0	DC		
G13.19−0.11	G13.185−0.109	53.3	HC	4.60 ±0.23	1.1 × 2.0
	G13.199−0.134	52.0	HC		
G13.22+0.03	G13.202+0.057	52.0	DC	4.57 ±0.22	8.0 × 3.1
	G13.216+0.029	52.0	HC		

[*]There are seven isolated sources which are not described in this table.

[†]Groups are named after the most luminous member in each group, but with fewer digits for the coordinates.

[‡]HC = HotCore; DC = DenseClump.

[§]We assume all sources in a group are at the same distance. See subsection 3.3 for the distance determination methods.

and Wu et al. (2014) for G14.636−0.569. We adopt these measurements as the most reliable distance estimates for these sources. For the sources that belong to the same groups as the above sources, we adopt the same distances because the spatial extent of the groups is small compared with the typical accuracy of the distance estimates. In this way, we assign trigonometric parallax-based distances to 13 HotCores and 3 DenseClumps.

For the remaining sources, we adopt the Bayesian distance proposed by Reid et al. (2014) that provides a probability distribution of distance that can explain the Galactic longitude and radial velocity of the source. Since the Bayesian distance is based on the kinematic distance, the method generally proposes two distances corresponding to the near and far side of the tangential point

in the region analyzed here. The distances of the far-side components are estimated to be as far as 13–15 kpc. In resolving this near/far ambiguity, we choose the distance of the near-side components because our survey is limited by the sensitivity of the FUGIN data, which make detection of distant objects difficult. The G10.18−0.35 group (W 31-South) and G10.300−0.144 (W 31-North) have spectrophotometric distance estimates of 3.55 kpc and 2.39 kpc, respectively, based on the near-infrared photometry of the embedded stellar clusters (Moisés et al. 2011). Our adopted distances agree with these estimates, considering the accuracies of the distance estimates: ∼1 kpc for the spectrophotometric method and ∼0.2 kpc for the Bayesian method. The negative velocity of the G11.11−0.39 group makes it tricky to determine its distance. In the
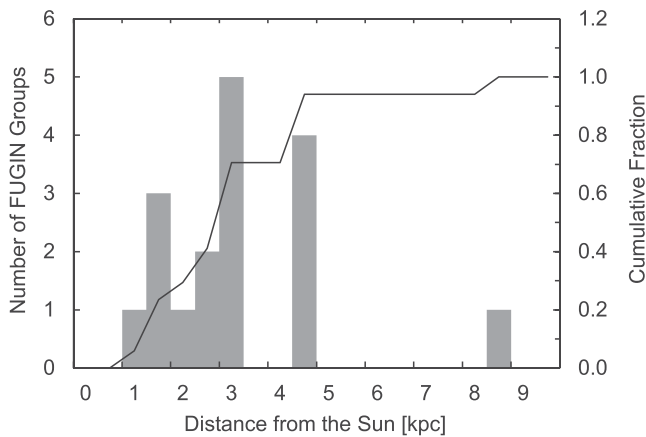
Fig. 6. Distance to the HotCores and DenseClumps from the Sun. Its cumulative fraction is also shown. We count a group of sources as one entity along with isolated sources.

longitude–velocity diagram of figure 5, the G11.11−0.39 group appears to be associated with the same arm-like structure as the G10.62−0.38 group, which has a trigonometric parallax distance. Consequently, we attribute to it the Bayesian distance close to the trigonometric parallax-based distance of the G10.62−0.38 group.

Figure 6 shows the distribution of the distances. Here we count a group of sources as one entity along with isolated sources. The histogram shows that most of the sources identified in this study are within 5 kpc of the Sun, with a typical distance of 3 kpc. This may represent the sensitivity limit of our hot core survey. One notable exception is the G10.47+0.03 group at $8.55^{+0.63}_{-0.55}$ kpc (Sanna et al. 2014), where we detect three very luminous HotCores.

4 Discussion

4.1 Nature of the FUGIN HotCores

What is the nature of the FUGIN HotCores and Dense-Clumps identified in this work? In this section we try to characterize them, particularly in the context of high-mass star formation.

4.1.1 Cross-matching with other signposts of high-mass star formation

First, we compare our list of FUGIN HotCores and Dense-Clumps with the published catalogs of signposts of high-mass star formation. Table 4 shows the result of cross-matching our catalog with the catalogs listed below.

ATLASGAL The APEX Telescope Large Area Survey of the Galaxy clumps have been identified from the 870 μm unbiased survey of the inner Galaxy with APEX and then followed up with millimeter-wave spectroscopic observations with a variety of telescopes (Urquhart et al. 2018). The list provides a large and systematic inventory of all massive, dense clumps in the Galaxy ($\geq 1000\,M_{\odot}$ at a heliocentric distance of 20 kpc) and includes representative samples of all of the earliest embedded stages of high-mass star formation. The original ATLASGAL survey was made with the APEX 12 m telescope with a 19″4 beam and a pointing accuracy of ∼4″ rms (Schuller et al. 2009).

Hi-GAL Herschel infrared Galactic Plane Survey compact sources at 70 μm are taken from the catalog presented by Molinari et al. (2016). The Herschel satellite has a 6″0 diffraction-limited beam at 70 μm, and the astrometric accuracy of the compact source catalog is estimated as ∼1″.

MMB The Methanol Multibeam Survey is a 6.7 GHz methanol maser survey with a positional accuracy of ∼0″4 (Green et al. 2010) and a 12.2 GHz follow-up survey (Breen et al. 2014). The observed maser lines are infrared pumped (Class II) and are expected in methanol-rich hot molecular gas illuminated by intense infrared radiation in high-mass star forming regions.

WISE H II regions This catalog of Galactic H II regions has been made from the all-sky mid-infrared (12 μm and 22 μm) data from the WISE satellite and cross comparison with radio-continuum surveys in the literature (Anderson et al. 2014). The angular resolution of the WISE images is 6″5 and 12″ for 12 μm and 22 μm, respectively. The catalog contains sources with a wide range of sizes from 6″ to >1000″.

CORNISH H II catalog This is an unbiased 5 GHz radio continuum survey of the inner Galactic plane using the Very Large Array coordinated with the Spitzer GLIMPSE survey (Hoare et al. 2012; Purcell et al. 2013). The survey detects emission on size scales from 1″5 up to 14″, thus emphasizing more compact H II regions compared with the WISE catalog. We refer to the list of "high reliability" (>7σ) sources identified as ultracompact H II regions or H II regions.

CS survey This is a CS $J = 2$–1 survey for dense molecular gas associated with the IRAS point sources with color characteristics of ultracompact H II regions (Bronfman et al. 1996). The observations were made with the OSO 20 m and SEST 15 m telescopes with angular resolutions of 39″ and 50″, respectively.

EGOA catalog of Extended Green Objects, this was a survey at 3.6 μm, 4.5 μm, 5.8 μm, 8.0 μm, and 24 μm for extended 4.5 μm objects (Cyganowski et al. 2008). Extended 4.5 μm emission may trace outflow and EGO sources correspond to high-mass star forming regions. The spatial resolution is within 2″ in all bands.

Table 4. Correspondence of HotCores and DenseClumps with other signposts of high-mass star formation.[*]

FUGIN	ATLASGAL clump[†]	Hi-GAL 70 μm[‡]	Methanol maser[§]	WISE H II region[‖]	CORNISH 5 GHz[♯]	IRAS/UCH II CS $J = 2$–1[**]	EGO[††]	L_{bol}/M_{clump}
HotCores								
G10.145−0.339	ON	ON	—	—	—	—	—	195
G10.178−0.350	ON	ON	—	—	—	—	—	126
G10.187−0.344	ON	NEAR	—	—	—	—	—	34.5
G10.220−0.369	ON	—	—	—	—	—	—	21.8
G10.300−0.144	ON	ON	ON	—	ON	NEAR	—	68.1
G10.465+0.034	ON	ON	—	ON	ON	ON	—	46.7[‡‡]
G10.473+0.028	NEAR	ON	ON	ON	ON	ON	—	46.7[‡‡]
G10.481+0.036	—	ON	ON	ON	—	NEAR	—	—
G10.623−0.380	ON	ON	NEAR	ON	ON	—	—	60.2
G11.920−0.616	ON	ON	—	NEAR	—	NEAR	ON	8.18
G11.939−0.616	ON	ON	ON	ON	ON	ON	—	32.8
G12.416+0.510	ON	NEAR	—	ON	—	ON	NEAR	18.5
G12.680−0.176	ON	NEAR	NEAR	NEAR	—	—	ON	9.20
G12.810−0.204	ON	ON	—	ON	ON	—	—	—
G12.888+0.490	ON	ON	ON	ON	—	ON	—	14.3
G13.185−0.109	ON	ON	—	ON	—	—	—	1.78
G13.199−0.134	NEAR	—	—	—	—	ON	—	20.8
G13.216+0.029	NEAR	—	—	—	—	—	—	—
G14.113−0.569	ON	ON	—	NEAR	—	—	—	0.931
G14.330−0.644	ON	ON	—	NEAR	—	NEAR	NEAR	8.07
G14.636−0.569	NEAR	—	—	—	—	—	NEAR	3.54
G19.367−0.041	NEAR	—	—	NEAR	—	—	NEAR	4.09
DenseClumps								
G10.131−0.408	ON	—	—	—	—	—	—	3.62
G10.195−0.397	NEAR	NEAR	—	NEAR	—	—	—	20.3
G10.203−0.341	ON	—	ON	NEAR	—	—	—	21.8
G10.203−0.308	NEAR	—	—	—	—	—	—	14.4
G10.209−0.336	NEAR	—	—	NEAR	—	—	—	21.7
G10.631−0.372	NEAR	ON	—	ON	—	—	—	60.3
G11.059−0.372	—	—	—	—	—	—	—	—
G11.109−0.388	NEAR	—	—	NEAR	NEAR	NEAR	—	9.71
G12.685−0.171	NEAR	—	—	NEAR	—	—	NEAR	9.20
G12.816−0.185	—	—	—	—	—	—	—	—
G12.855−0.201	ON	—	—	—	—	—	—	2.52
G12.911+0.487	ON	NEAR	—	ON	—	—	—	7.78
G13.202+0.057	—	NEAR	—	—	—	—	—	—
G14.202−0.199	ON	—	—	—	—	—	—	1.19

[*]ON = correspondence within 20″ for the Hi-GAL sources and methanol masers, and within 30″ for the other sources; NEAR = correspondence with a position error of 20″–30″ for the Hi-GAL sources and methanol masers, and 30″–60″ for the other sources.

[†]ATLASGAL 870 μm clumps with molecular line follow-ups (Urquhart et al. 2018).

[‡]70 μm compact sources with >50 Jy in the Herschel Hi-GAL survey (Molinari et al. 2016).

[§]Class II methanol masers found in the 6.7 GHz Methanol Multibeam Survey (Green et al. 2010).

[‖]Galactic H II regions identified in mid-infrared by WISE (Anderson et al. 2014).

[♯]"High reliability" 5 GHz sources identified as ultracompact H II regions or H II regions (Purcell et al. 2013).

[**]CS $J = 2$–1 sources detected toward the IRAS point sources with color characteristics of ultracompact H II regions (Bronfman et al. 1996).

[††]Extended 4.5 μm object (Cyganowski et al. 2008).

[‡‡]Same ATLASGAL clump (AGAL 010.462+0.031) selected as counterpart of two FUGIN HotCores.

When the objects identified by various observational probes have a range of scale sizes, their cross matching is not straightforward in general. This is true in our situation. We identify the counterparts with the following criteria: (i) Positional agreement at the level of <30″ (0.44 pc at 3 kpc) for Hi-GAL, CH$_3$OH maser, and CORNISH sources, and <60″ for the other sources. (ii) Source compactness at the level of 10′. This is because we are interested in
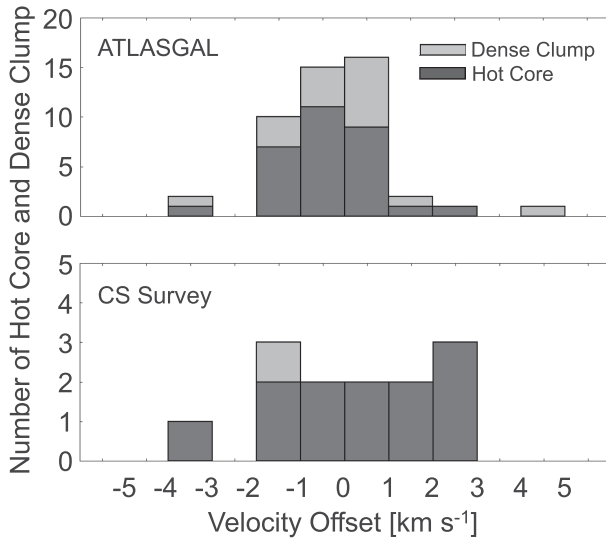
Fig. 7. Histogram of velocity offset between our sources and other catalog sources. The upper panel shows the result with ATLASGAL (Urquhart et al. 2018) and the lower panel shows the result with CS sources (Bronfman et al. 1996).

closer spatial coincidence and physical relationship with our sources (see subsection 3.1). (iii) Radial velocities coincident within $\approx 5\,\mathrm{km\,s^{-1}}$ when available. Figure 7 shows the offsets of the peak velocities of the identified ATLASGAL and CS survey sources. The median values of velocity offset are $-0.2\,\mathrm{km\,s^{-1}}$ for ATLASGAL and $-0.3\,\mathrm{km\,s^{-1}}$ for CS sources. In the case of MMB methanol masers, we require the peak velocity of our sources to fall within the velocity range of the maser emission.

ATLASGAL clumps are often extended and overlap with each other, and this makes it difficult to uniquely identify the counterparts of FUGIN HotCores from the coordinates only. In such cases we refer to the ATLASGAL image and select clumps that show a better match with the HotCore by visual inspection. We find ATLASGAL clumps ON or NEAR 21 (95%) of the 22 FUGIN HotCores. In the case of HotCores G10.465+0.034 and G10.473+0.028, we select the clump AGAL 10.462+0.031 for the counterpart of both HotCores because the two HotCores appear to be embedded in the single continuous ATLASGAL clump.

Hi-GAL $70\,\mu\mathrm{m}$ sources are found ON or NEAR 17 (77%) of the FUGIN HotCores.

As for the association with H II regions, 16 (73%) of the FUGIN HotCores have their H II region counterparts as indicated by the WISE, CORNISH, and/or IRAS/UCH II CS catalogs. The CORNISH catalog provides a list of ultra-compact and compact H II regions that are in more direct physical interaction with the HotCores, while the WISE catalog includes more extended H II regions showing the physical environment surrounding the HotCores as well. We find 6 HotCores (27%) directly associated with the

CORNISH H II regions. Methanol masers at 6.7 GHz are found ON or NEAR 7 HotCores (32%). These coincidences, along with the association with the Hi-GAL $70\,\mu\mathrm{m}$ sources, suggest that these FUGIN HotCores are similar in nature to the classical hot cores associated with massive star formation.

At the same time, we note that many HotCores do not show clear association with H II regions. Some HotCores may be associated with EGOs found nearby (G14.330−0.644, G14.636−0.569, G19.367−0.041), which may hint at earlier stages of star formation or formation of less massive stars resulting in radio-quiet infrared sources. We also note that some HotCores are in the mini-starburst region W 31 (G10.145−0.339, G10.178−0.350, G10.187−0.344, G10.220−0.369), and confusion with structures in the H II region complex could have hindered the identification of associated compact H II regions.

For the remaining 13 candidates categorized as FUGIN DenseClumps, we find 11 ATLASGAL clumps ON or NEAR the position of the DenseClumps (85%), but they exhibit generally much less coincidence with the other signposts of massive star formation compared with the FUGIN HotCores.

Four of the FUGIN HotCores (G10.473+0.028, G10.623−0.380, G11.939−0.616, and G12.888+0.490) are already known as classical hot cores (see, e.g., Rolffs et al. 2011).

4.1.2 Identification with Hi-GAL clumps with mass and luminosity estimates

Another important database on potential sites of star formation is the clump catalog made from the Herschel Hi-GAL survey (Elia et al. 2017). It is a band-merged catalog of spatially matched sources detected in at least three consecutive wavelength bands of 160, 250, 350, and $500\,\mu\mathrm{m}$, along with their properties derived from fits to the spectral energy distributions (SEDs). The sources are classified as *prestellar* or *protostellar*, mainly by the SED.

Table 5 shows the result of the cross matching between the Hi-GAL clumps and the FUGIN HotCores and Dense-Clumps. Sixteen out of the 22 FUGIN HotCores have been identified with the Hi-GAL clumps. Most of them exhibit SEDs classified as *protostellar*, as we expect from frequent coincidence with the Hi-GAL $70\,\mu\mathrm{m}$ sources. Three bright HotCore sources, G10.473+0.028, G10.623−0.380, and G12.810−0.204, are not included in the Hi-GAL clump catalog because a reliable SED cannot be constructed due to detector saturation, but it is probable that these sources would have been included as *protostellar* sources in the Hi-GAL clumps if the saturation had not occurred. We are impressed by the high rate of identification (16/19

Table 5. Bolometric luminosity and other parameters of HotCores and DenseClumps.

FUGIN	Positional coincidence*	M_{clump} $[M_\odot]$	T_{dust} [K]	T_{bol} [K]	L_{bol} $[L_\odot]$	Hi-GAL	Evolutionary classification[†]
HotCores							
G10.178−0.350	ON	3.4×10^2	23.3	25.0	3.1×10^3	HIGALBM10.1764−0.3502	2
G10.187−0.344	ON	6.4×10^2	18.6	27.1	2.1×10^3	HIGALBM10.1912−0.3468	1
G10.220−0.369	NEAR	1.9×10^2	20.2	25.7	9.8×10^2	HIGALBM10.2218−0.3628	2
G10.300−0.144	ON	9.6×10^2	28.2	51.1	3.3×10^4	HIGALBM10.3013−0.1471	2
G10.465+0.034	ON	2.3×10^3	24.7	46.3	6.0×10^4	HIGALBM10.4631+0.0298	2
G10.481+0.036	ON	2.8×10^3	23.6	50.9	2.1×10^5	HIGALBM10.4809+0.0333	2
G11.920−0.616	ON	7.5×10^2	24.2	45.3	1.5×10^4	HIGALBM11.9181−0.6123	2
G11.939−0.616	ON	4.2×10^2	40.0	56.0	5.9×10^4	HIGALBM11.9370−0.6159	2
G12.416+0.510	NEAR	1.1×10^2	38.8	58.9	1.1×10^4	HIGALBM12.4177+0.5043	2
G12.680−0.176	NEAR	7.2×10^2	19.6	44.9	5.8×10^3	HIGALBM12.6805−0.1819	2
G12.888+0.490	ON	4.1×10^2	33.4	45.2	1.7×10^4	HIGALBM12.8892+0.4895	2
G13.185−0.109	ON	9.6×10^2	17.1	51.6	8.5×10^3	HIGALBM13.1836−0.1064	2
G13.199−0.134	ON	1.3×10^3	20.5	30.1	6.3×10^3	HIGALBM13.2034−0.1360	2
G13.216+0.029	ON	5.9×10^3	10.5	14.7	5.4×10^2	HIGALBM13.2175+0.0322	1
G14.113−0.569	ON	3.7×10^2	16.7	26.5	6.1×10^2	HIGALBM14.1136−0.5745	2
G14.330−0.644	ON	1.9×10^2	25.7	31.4	1.5×10^3	HIGALBM14.3314−0.6436	2
DenseClumps							
G10.131−0.408	ON	2.6×10^2	16.1	23.7	3.8×10^2	HIGALBM10.1320−0.4110	1
G12.855−0.201	NEAR	1.5×10^2	17.3	25.5	3.2×10^2	HIGALBM12.8574−0.2073	1
G12.911+0.487	NEAR	1.2×10^2	19.3	31.7	5.4×10^2	HIGALBM12.9154+0.4934	2

*ON = correspondence within 20″; NEAR = correspondence with a position error of 20″–30″.

[†]1: prestellar; 2: protostellar (Elia et al. 2017).

or 84% except for the saturated sources) between the FUGIN HotCores and the Hi-GAL clumps. In contrast, we identify only 3 out of the 13 DenseClumps with Hi-GAL clumps.

For the clump mass and the bolometric luminosity, Elia et al. (2017) list those estimated by temporarily adopting a distance of 1 kpc in view of the distance ambiguities. Since we have estimated the distances of the FUGIN HotCores and DenseClumps in subsection 3.3, the values in table 5 have been scaled for the distances in table 2. The mass of the Hi-GAL clumps identified with FUGIN HotCores is $1.1 \times 10^2 \, M_\odot$ to $5.9 \times 10^3 \, M_\odot$ with a median of $6.8 \times 10^2 \, M_\odot$, large enough to form a cluster including massive ($\geq 8 \, M_\odot$) stars. Their bolometric luminosity ranges from $5.4 \times 10^2 \, L_\odot$ to $2.1 \times 10^5 \, L_\odot$ with a median of $7.4 \times 10^3 \, L_\odot$. Ten out of the 16 Hi-GAL clumps identified with FUGIN HotCores have bolometric luminosities higher than that of an $8 \, M_\odot$ zero-age main sequence (ZAMS) star, $4 \times 10^3 \, L_\odot$ (see, e.g., Wang & Zhong 2018). Even the least luminous source, G13.216+0.029, has a luminosity comparable to a $4.8 \, M_\odot$ ZAMS star. All these observations suggest that the FUGIN HotCores are closely related to formation of stars with medium to high mass, and it is quite probable that some of them actually have classical hot cores embedded in them.

4.1.3 Gas temperature estimates

In some FUGIN HotCore sources we have detected multiple lines of CH_3CN that arise from energy levels of different K at a range of energies from the ground state (table 1). From the symmetric top nature of CH_3CN, its radiative transitions are allowed only for those that do not alter K, i.e., within the same K-ladder, and the relative population between the different K-ladders is largely determined by collisions. This makes CH_3CN a good probe to estimate the temperature of dense gas (see, e.g., Remijan et al. 2004 and references therein).

We make an attempt to estimate the gas temperature for the following seven HotCore sources with CH_3CN intensities greater than $5 \, \mathrm{K \, km \, s^{-1}}$ in the blended $K = 0, 1$ lines: G10.300−0.144, G10.473+0.028, G10.623−0.380, G11.920−0.616, G12.810−0.204, G12.888+0.490, and G14.330−0.644. From all these seven sources we have detected the $K = 2$ and $K = 3$ lines, so that we have line intensity ratios $I_{K=2}/I_{K=0, 1}$ and $I_{K=3}/I_{K=0, 1}$, where $I_{K=2}$, $I_{K=3}$, and $I_{K=0, 1}$ are the integrated intensities of the $K = 2$, $K = 3$, and the blend of the $K = 0, 1$ lines, respectively. G10.473+0.028 is exceptionally intense in CH_3CN, and we also detected the $K = 4$ and $K = 5$ lines as well as the $K = 0, 1$ blend of $CH_3^{13}CN$. The line intensity ratios in G10.473+0.028 suggest that this source has a large optical

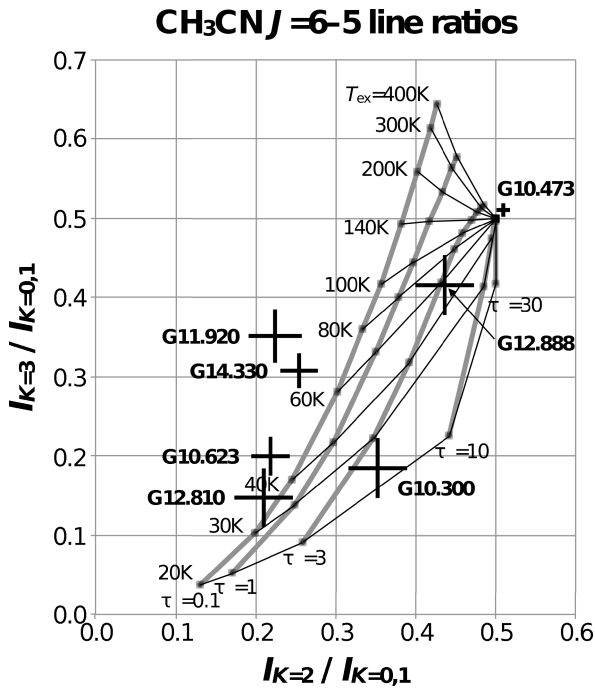## CH₃CN *J* =6–5 line ratios

Fig. 8. Intensity ratios of the CH₃CN $J = 6–5$ lines, $I_{K=2}/I_{K=0,1}$ and $I_{K=3}/I_{K=0,1}$, observed from the seven HotCore sources. Also shown are the line intensity ratios expected for the one-zone LTE model at the rotational excitation temperature T_{ex} (black lines), and the optical depth of the $J_K = 6_0–5_0$ line, τ (gray lines).

depth of $\tau \approx 15$ in the CH₃CN $J_K = 6_0–5_0$ line[2] and the rotational excitation temperature is $T_{ex} \approx 100$ K, based on the one-zone local thermal equilibrium (LTE) model described below.

Figure 8 shows the ratios $I_{K=2}/I_{K=0,1}$ and $I_{K=3}/I_{K=0,1}$ observed from the seven sources, in comparison with those expected for a one-zone LTE model. In the model we assume that all the relevant energy levels are populated in LTE at a rotational excitation temperature T_{ex}, and that the source has the optical depth of the $J_K = 6_0–5_0$ line τ. For the six sources other than G10.473+0.028, 3σ upper limits of τ < 2.5–5.5 are given from the non-detection of the CH₃¹³CN lines. We also make a one-zone assumption that the physical conditions are uniform over the emitting region, which is smaller than the observing beam, and that the beam filling factor of a given source is the same for all the observed lines.

The above analysis of the CH₃CN line ratios suggests that the gas temperature of the CH₃CN-emitting region may vary between sources from 20–40 K (G10.300−0.144, G12.810−0.204)   to   50–100 K   (G10.623−0.380, G12.888+0.490,   G14.330−0.644,   G11.920−0.616,

G10.473+0.028).[3] These temperatures are lower than the nominal gas temperature of a classical hot core, $T > 100$ K. This could be partly due to our analysis with the LTE assumption, which tends to underestimate the temperature (Remijan et al. 2004). Indeed, consulting the non-LTE calculations of RADEX (Van der Tak et al. 2007) suggests that the intensity ratios of the lines observed from G10.473+0.028 are better fitted with a higher temperature of ∼150–200 K. We should also keep in mind that the present estimate is based on line intensities observed with a 14″ beam that is larger than the typical size of a classical hot core (<0.1 pc or <7″ at a distance of 3 kpc). This could cause an underestimate of the temperature in the central core region if the temperature and density drop with the distance from the exciting source. Thus, the temperature estimates in the present study may be viewed as lower limits.

We have also detected multiple lines of CH₃OH. Among them, the only line arising from a relatively high energy level is $J_K = 8_0–7_1$ A⁺ at 95.169 GHz (table 1). Although the potential maser nature of this line makes quantitative analysis difficult, it is intriguing to note in table 2 that the intensity of the 8–7 line relative to the 2–1 lines correlates with the temperature estimated from CH₃CN. The 8–7/2–1 ratio is higher (0.2–1.1) for the five sources with higher CH₃CN temperatures of 50–100 K, while the ratio is ≈0.1 or lower for the rest of the sources. The higher 8–7/2–1 ratio may indicate that the gas temperature and/or the CH₃OH column density are elevated in the former group of sources.

Follow-up observations of the HotCore sources with higher spatial resolution and sensitivity including more lines from even higher energy levels are needed to improve the accuracy of the temperature estimates.

4.1.4 Evolutionary stage of the FUGIN HotCores
We saw that many of the FUGIN HotCores appear to show close relationships with high-mass star formation. Now we discuss their evolutionary stages.

From studying the ATLASGAL-selected massive clumps, Giannetti et al. (2017) showed that the ratio of bolometric luminosity to clump mass statistically correlates with the evolutionary stage of the clump. Bolometric luminosity over clump mass (L_{bol}/M_{clump}) increases as the star formation stage evolves. Sources with $L_{bol}/M_{clump} < 2\,L_\odot/M_\odot$ are considered as still accumulating sources, those with $2\,L_\odot/M_\odot \leq L_{bol}/M_{clump} \leq 40\,L_\odot/M_\odot$ as young stellar

---

[2] We assume a ¹²CO/¹³CO abundance ratio of 40 and LTE to estimate the optical depth, τ.

[3] In figure 8 we note marginal (2σ to 2.5σ) discrepancies between the observed ratios of some sources and the range of the ratios expected from the LTE model. We cannot tell, from the data in hand at present, whether this is simply due to random noise or an indication of a systematic departure from the conditions assumed in the model.
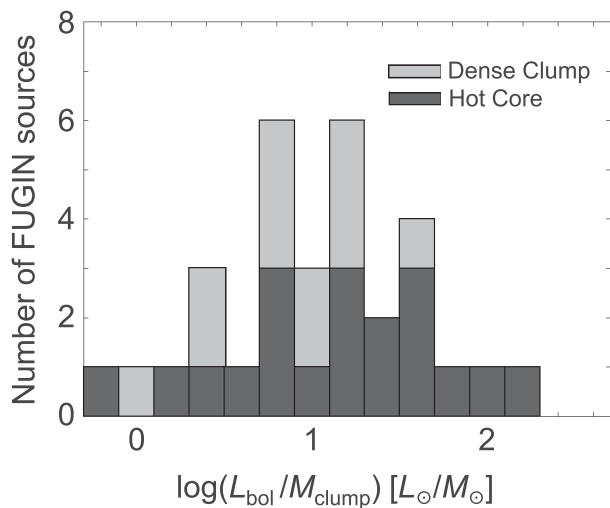
Fig. 9. Histogram of L_{bol}/M_{clump} for FUGIN HotCores and DenseClumps.

objects (YSOs) or ZAMS stars and hot cores, and those with $L_{bol}/M_{clump} > 40\,L_\odot/M_\odot$ as H II regions.

Figure 9 shows the distribution of L_{bol}/M_{clump} ratios of the FUGIN HotCores and DenseClumps. The L_{bol}/M_{clump} are taken from the values for the corresponding ATLASGAL clumps listed in Urquhart et al. (2018). Eleven out of the 21 FUGIN HotCores (52%) exhibit a L_{bol}/M_{clump} ratio between 2 and $40\,L_\odot/M_\odot$, suggesting that they are statistically in the stage of YSOs or ZAMS stars and hot cores. This is in agreement with our conclusion that about 1/3 to 2/3 of the FUGIN HotCores are similar in nature to classical hot cores. On the other hand, the larger spread in the L_{bol}/M_{clump} distribution beyond the 2–40 $L_\odot/M_\odot$ range suggests that the FUGIN HotCores may also include objects in evolutionary stages earlier or later than that of the classical hot cores.

4.2 Limitations of this survey

As described in subsection 2.1, our survey of hot cores starts by finding source candidates in the FUGIN data. Since the sensitivity of the FUGIN survey has been set for its original purpose of a Galactic survey in the ^{12}CO, ^{13}CO, and $C^{18}O$ lines, the signal-to-noise ratios for the weaker HNCO and CH$_3$CN lines we seek as hot core signatures are not very high. The noise varies typically by a factor of two from one degree squared region to another due to the varying observing conditions and available time during the original FUGIN observations. In addition, the stability of the four receivers corresponding to the four beams of FOREST was uneven during the observations, leaving strong scanning patterns in the maps in some regions. Here we examine the limitations of the present results and cautions concerning their use caused by this non-ideal situation.

Since we have set the detection limit for the stacked HNCO and CH$_3$CN lines at 5σ (0.1–0.2 K) referring to the noise level of the individual stacked spectra,[4] the sensitivity limit for the candidate sources is uneven. Nevertheless, we report all the detected HotCores and DenseClumps in this paper because it has the merit of increasing the number of sources at this stage of the research. We can impose additional selection criteria to get a subset from the present list if our analysis requires a sample with a better-controlled sensitivity limit.

The positional accuracy of the sources is also limited by the relatively low signal-to-noise ratio. The maps we use in the candidate selection have been made with a 10″ grid using a gridding convolution function that corresponds to a half power beam width of ~20″ (Sawada et al. 2008). This limits the positional accuracy in the first place. When the signal-to-noise ratio is low, the noise fluctuation may cause a positional error of one pixel (10″) in l or b. When we have two or more detections at spatially adjacent pixels, we take the position of the strongest intensity of the stacked HNCO and CH$_3$CN lines as the position of the candidate. This can introduce further positional error if the source is actually a marginally resolved cluster (i.e., source confusion) or the intensity distribution is distorted by the noise. With these limitations, we expect that the errors of the source position are about 10″, with some cases getting even larger.

Among the objects used in the cross-matching in sub-subsection 4.1.1, the Hi-GAL 70 μm source and the MMB 6.7 GHz methanol masers are compact in size and have high positional accuracy of the order of an arcsecond. Out of the 17 Hi-GAL 70 μm sources exceeding 50 Jy found within 30″ of the nominal position of the FUGIN HotCores, 7 (41%) and 14 (82%, cumulative) are within 10″ and 20″ of the HotCore positions, respectively. Similarly, of the 7 MMB methanol maser sources, 3 (43%) and 5 (71%, cumulative) are found within 10″ and 20″ of the HotCore positions, respectively. These counts may overestimate the scatter of the positional error, because the measured values reflect projected distance, and because the counts may be slightly contaminated by foreground and background sources in the Galactic disk by chance coincidence. This is consistent with our expectations that the positional accuracy of the FUGIN HotCores is about 10″ with possible errors larger than 20″ for some sources.

As a result of the sensitivity limit and positional errors that may also have affected the confirmation observations, we have missed some real sources. For example, in the ATLASGAL-based spectral-line follow-up [Millimetre

---

[4] By doing so, we can reduce false candidate detection caused by the scanning effect, because the spectra with the scanning effect have higher rms noise.

Astronomy Legacy Team 90 GHz (MALT90) survey], Rathborne et al. (2016) detected seven sources of CH_3CN emission exceeding $T_A^* = 0.15$ K with the Mopra 24 m telescope in the area of the present survey. Four of them are identified as HotCores in our survey, while we missed three sources: AGAL 12.904−0.031, AGAL 13.178+0.059, and AGAL 14.777−0.487. In using the FUGIN HotCore survey results, we need to keep in mind the possibility of missed sources.

5 Summary

We have developed a method to survey hot cores without bias to continuum emission by using the FUGIN data. We first listed hot core candidates based on the $C^{18}O$ $J = 1$–0 and the stacked HNCO $J_{K_a, K_c} = 5_{0,5}$–$4_{0,4}$ plus CH_3CN $J = 6$–5 line intensities and their distribution in the FUGIN datacube. We then conducted more sensitive follow-up observations of the candidates in hot core tracer lines by using the Nobeyama 45 m telescope to confirm and characterize the identified objects. The observed lines include $C^{34}S$ $J = 2$–1, SO $J_K = 2_3$–1_2, OCS $J = 9$–8, HC$_3$N $J = 12$–11, and CH_3OH $J = 2$–1 and $J = 8$–7, in addition to the $C^{18}O$ $J = 1$–0, HNCO $J_{K_a, K_c} = 5_{0,5}$–$4_{0,4}$, and CH_3CN $J = 6$–5 lines used in the candidate selection. We define FUGIN HotCores as sources of spatially compact ($\ll 100''$) emission detected above 3σ in at least two of the hot core tracer lines. We also detect DenseClumps which do not meet the HotCore criteria but have at least two lines that indicate high molecular gas density.

We have applied this method to the 17 degrees squared area in the $l = 10°$–$20°$ region of the FUGIN survey, and identified 22 HotCores and 14 DenseClumps. The main findings from the initial analysis of these sources are summarized as follows:

1. Most of the identified HotCores and DenseClumps are within 5 kpc of the Sun, with a typical distance of 3 kpc. This may represent the sensitivity limit of the survey.
2. Many of the sources are clustered in groups of ∼1–10 pc in diameter, showing that formation of high-mass stars proceeds concurrently at multiple locations within this spatial scale. The spatial extent and the velocity spread of cores within each group is roughly in agreement with the size–linewidth relation of interstellar molecular clouds (Larson 1981).
3. Many of the FUGIN HotCores have counterparts in signposts of star formation such as ATLASGAL dust clumps (95%), WISE H II regions (64%), and Class II methanol masers (32%). We identify 84% of FUGIN HotCores with Herschel Hi-GAL clumps with a median

mass of $6.8 \times 10^2 M_\odot$ and a median bolometric luminosity of $7.4 \times 10^3 L_\odot$. This suggests that FUGIN Hot-Cores are closely related to the formation of stars with medium to high mass. It is likely that some of them have actually have classical hot cores.

4. We estimated gas temperatures for seven HotCores from multiple CH_3CN lines using a one-zone LTE model. Five of the sources exhibit elevated gas temperatures of 50–100 K. These temperature estimates are viewed as lower limits.
5. For the HotCores with ATLASGAL counterparts, we found their bolometric luminosity to clump mass ratios, L_{bol}/M_{clump}, which range from ∼1 $L_\odot/M_\odot$ to ∼$10^2 L_\odot/M_\odot$. About 2/3 of them fall within the range of 2–40 $L_\odot/M_\odot$ that statistically corresponds to the stages of accreting protostars, ZAMS stars, and hot cores (Giannetti et al. 2017). The FUGIN HotCore sample is closely related to the classical hot cores, but may cover a somewhat broader range of star formation stages than the classical hot core phase.

On the basis of the results described in this paper, we are expanding the analysis and corresponding confirmation observations to the $l = 20°$–$50°$ part of the FUGIN data, with the aim of completing the catalog of FUGIN HotCores for the first Galactic quadrant. This would significantly increase the number of HotCores available for statistical analysis of their evolution and chemistry. The catalog would also provide a useful starting point for high-resolution studies of the physical and chemical structures of a sample of high-mass star forming regions with ALMA.

Acknowledgments

References

Anderson, L. D., Bania, T. M., Balser, D. S., Cunningham, V., Wenger, T. V., Johnstone, B. M., & Armentrout, W. P. 2014, ApJS, 212, 1

Bisschop, S. E., Jørgensen, J. K., van Dishoeck, E. F., & de Wachter, E. B. M. 2007, A&A, 465, 913

Breen, S. L., et al. 2014, MNRAS, 438, 3368

Bronfman, L., Nyman, L.-A., & May, J. 1996, A&AS, 115, 81

Chen, X., Ellingsen, S. P., Shen, Z.-Q., Titmarsh, A., & Gan, C.-G. 2011, ApJS, 196, 9

Cyganowski, C. J., et al. 2008, AJ, 136, 2391

Elia, D., et al. 2017, MNRAS, 471, 100

Giannetti, A., Leurini, S., Wyrowski, F., Urquhart, J., Csengeri, T., Menten, K. M., König, C., & Güsten, R. 2017, A&A, 603, A33

Green, J. A., et al. 2010, MNRAS, 409, 913

Hatchell, J., Fuller, G. A., Millar, T. J., Thompson, M. A., & Macdonald, G. H. 2000, A&A, 357, 637

Hoare, M. G., et al. 2012, PASP, 124, 939

Immer, K., Reid, M. J., Menten, K. M., Brunthaler, A., & Dame, T. M. 2013, A&A, 553, A117

Kuno, N., et al. 2011, in Proc. 2011 XXXth URSI General Assembly and Scientific Symp., Vol. 1 (New York: IEEE), 3670

Larson, R. B. 1981, MNRAS, 194, 809

Minamidani, T., et al. 2016, SPIE Proc., 9914, 99141Z

Moisés, A. P., Damineli, A., Figuerêdo, E., Blum, R. D., Conti, P. S., & Barbosa, C. L. 2011, MNRAS, 411, 705

Molinari, S., et al. 2016, A&A, 591, A149

Nomura, H., & Millar, T. J. 2004, A&A, 414, 409

Purcell, C. R., et al. 2013, ApJS, 205, 1

Rathborne, J. M., et al. 2016, PASA, 33, e030

Reid, M. J., et al. 2014, ApJ, 783, 130

Remijan, A., Sutton, E. C., Snyder, L. E., Friedel, D. N., Liu, S.-Y., & Pei, C.-C. 2004, ApJ, 606, 917

Rolffs, R., Schilke, P., Zhang, Q., & Zapata, L. 2011, A&A, 536, A33

Sanna, A., et al. 2014, ApJ, 781, 108

Sato, M., et al. 2014, ApJ, 793, 72

Sato, M., Hirota, T., Reid, M. J., Honma, M., Kobayashi, H., Iwadate, K., Miyaji, T., & Shibata, K. M. 2010, PASJ, 62, 287

Sawada, T., et al. 2008, PASJ, 60, 445

Schuller, F., et al. 2009, A&A, 504, 415

Umemoto, T., et al. 2017, PASJ, 69, 78

Urquhart, J. S., et al. 2018, MNRAS, 473, 1059

van der Tak, F. F. S., Black, J. H., Schöier, F. L., Jansen, D. J., & van Dishoeck, E. F. 2007, A&A, 468, 627

Wang, J., & Zhong, Z. 2018, A&A, 619, L1

Wu, Y. W., et al. 2014, A&A, 566, A17

Wyrowski, F., Menten, K. M., Schilke, P., Thorwirth, S., Güsten, R., & Bergman, P. 2006, A&A, 454, L91

Xu, Y., Moscadelli, L., Reid, M. J., Menten, K. M., Zhang, B., Zheng, X. W., & Brunthaler, A. 2011, ApJ, 733, 25

Yamamoto, S. 2017, Introduction to Astrochemistry: Chemical Evolution from Interstellar Clouds to Star and Planet Formation (Tokyo: Springer)